Large-eddy simulation of radiation fog with comprehensive two-moment bulk microphysics: Impact of different aerosol activation and condensation parameterizations

Johannes Schwenkel[1] and Björn Maronga[1,2]

[1]Institute of Meteorology and Climatology, Leibniz Universität Hannover, Hannover, Germany
[2]Geophysical Institute, University of Bergen, Bergen, Norway

Correspondence to: Johannes Schwenkel (schwenkel@muk.uni-hannover.de)

Abstract. In this paper we study the influence of the cloud microphysical parameterization, namely the effect of different treatment of diffusional growth and aerosol activation, on the structure and life cylce of radiation fog in large-eddy simulations. For this purpose we investigate a selected deep fog case as observed at Cabauw (Netherlands) using high-resolution large-eddy simulations with comprehensive bulk cloud microphysics scheme. By comparing saturation adjustment with an explicit and a prognostic method for calculating supersaturation (while neglecting the activation process) we find that, even though assumptions for saturation adjustment are violated, the expected overestimation of the liquid water mixing ratio is negligible. By additionally considering activation, however, our results indicate that saturation adjustment, due to approximating the underlying supersaturation, leads to a higher droplet concentration and hence significantly higher liquid water content in the fog layer, while explicit and prognostic methods yield comparable results. Furthermore, the effect of different droplet number concentrations is investigated, induced by using different common activation schemes. We find, in line with previous studies, a positive feedback between the droplet number concentration and strength of the fog layer (defined by its vertical extent and amount of liquid water). Furthermore, we perform an explicit analysis of the budgets of condensation, evaporation, sedimentation and advection in order to assess which processes have the largest spatial influence on the development of the fog layer in its different development phases.

1 Introduction

The prediction of fog is an important part of the estimation of hazards and efficiency in traffic and economy (Bergot, 2013). The annual damage caused by fog events is estimated to be the same as the amount caused by winter storms (Gultepe et al., 2009). Despite improvements in numerical weather prediction (NWP) models, the quality of fog forecasts is still unsatisfactory. The explanation for this is obvious: fog is a meteorological phenomenon influenced by a multitude of complex physical processes. Namely, these processes are radiation, turbulence, atmosphere-surface interactions, and cloud microphysics (hereafter referred to as microphysics), and which interact on different scales (e.g. Gultepe et al., 2007; Haeffelin et al., 2010). The key issue for improving fog prediction in NWP models is to resolve the relevant processes explicitly, or - if that is not possible - to parameterize them in an appropriate way.

In recent years various studies have focused on the influence of microphysics on fog. In particular, the activation of aerosols (hereafter simply referred to as activation), which determines how many aerosols at a certain supersaturation get activated and hence can grow into cloud drops, is a key process and thus of special interest (e.g. Bott, 1991; Hammer et al., 2014; Boutle et al., 2018).

Stolaki et al. (2015) investigated and compared the influence of aerosols on the life cycle of a radiation fog event while using the one-dimensional mode of the MESO-NH model with a two-moment warm microphysics scheme after Geoffroy et al. (2008) and Khairoutdinov and Kogan (2000) and included an activation parameterization after Cohard et al. (1998). In other fog studies, using single-column models, different activation schemes such as the simple Twomey-power law activation in Bott and Trautmann (2002) and the scheme of Abdul-Razzak and Ghan (2000) (see Zhang et al., 2014) were applied. Furthermore, also more advanced methods such as sectional models have been used for an appropriate activation representation. Maalick et al. (2016) used the Sectional Aerosol module for Large Scale Applications (SALSA) (Kokkola et al., 2008) in two-dimensional studies for a size-resolved activation. Mazoyer et al. (2017) conducted similar to Stolaki et al. (2015) simulation of the ParisFog with the MESO-NH model but using the 3D-Large-Eddy Simulation (LES) mode, and focusing on the influence of drag effect on droplet deposition. For the fog microphysics they also used an activation parameterizations after Cohard et al. (2000) in connection with saturation adjustment. This large number of different activation parameterizations raises the question how different methods affect the structure and life cycle of radiation fog. Furthermore, schemes that parameterize activation based on updrafts might fail for fog. Such schemes derive supersaturation as a function of vertical velocity, which is valid for convective clouds that are forced by surface heating, but not for radiation fog, which is mainly driven by longwave radiative cooling in its mature phase (Maronga and Bosveld, 2017; Boutle et al., 2018).

Although great progress has been made to understand different microphysical processes in radiation fog based on numerical experiments, turbulence as a key process has been either fully parameterized (single-column models) or oversimplified (two-dimensional LES). Since turbulence is a fundamentally three-dimensional process, the full complexity of all relevant mechanisms can only be reproduced with three-dimensional LESs (Nakanishi, 2000).

Moreover, a disadvantage of most former studies is the use of saturation adjustment, which implies that supersaturations are immediately removed within one time step. This approach is only valid when the time scale for diffusion of water vapour (on order of 2-5 s) is much smaller than the model time step, which is the case in large scale models where time steps are on the order of 1 min. However, in LES of radiation fog, time steps easily go down to split seconds so that this assumption is violated and might lead to excessive condensation (e.g. Lebo et al., 2012). Following Lebo et al. (2012) and Thouron et al. (2012), who investigated the influence of different supersaturation calculations for deep convective cloud and stratocumulus, the present work considers the effect of saturation adjustment on radiation fog.

As Mazoyer et al. (2017) and Boutle et al. (2018) stated that both, LES and NWP models tend to overestimate the liquid water content and the droplet number concentration for radiation fog the following questions are derived from these shortcomings:

(i) Is saturation adjustment appropriate as it crucially violates the assumption of equilibrium? How large is the effect of different supersaturation calculations on diffusional growth?

(ii) What is the impact of different activation schemes on the fog life cycle for a given aerosol environment?

(iii) As the number of activated droplets is essentially determined by the supersaturation, how large is the effect of different supersaturation modeling approaches on aerosol activation and therewith on the strength and life cycle of radiation fog (cf. Thouron et al., 2012)?

In the present paper we will address the above issues by employing high-resolution LESs based on an observed typical deep fog event with continental aerosol conditions.

The paper is organized as follows: Section 2 outlines the methods used, that is the LES modeling framework and the microphysics parameterizations used. Section 3 provide an overview of the simulated cases and model setup, while results are presented in section 4. Conclusions are given in section 5.

2 Methods

This section will outline the used LES model and the treatment of radiation and land-surface interactions, followed by a more detailed description of the bulk microphysics implemented in the Parellized Large-Eddy Simulation Model (PALM) and the extensions made in the scope of the present study.

2.1 LES model with embedded radiation and land surface model

In this study the LES model PALM (Maronga et al. 2015; revision 2675 and 3622) was used with extensions in the microphysics parameterizations. PALM has been successfully applied to simulate the stable boundary layer (BL) (e.g. during the first intercomparison of LES for stable BL, GABLS, Beare et al., 2006) as well as radiation fog (Maronga and Bosveld, 2017). The model is based on the incompressible Boussinesq-approximated Navier-Stokes equations, and prognostic equations for total water mixing ratio, potential temperature, and subgrid-scale turbulence kinetic energy. PALM is discretized in space using finite differences on a Cartesian grid. For the non resolved eddies a 1.5-order flux-gradient subgrid closure scheme after Deardorff (1980) is applied, which includes the solution of an additional prognostic equation for the subgrid-scale TKE. Moreover, the discretization for space and time is done by a fifth-order advection scheme after Wicker and Skamarock (2002) and a third-order Runge-Kutta time-step scheme (Williamson, 1980), respectively. The interested reader is referred to Maronga et al. (2015) for a detailed description of the PALM model.

In order to account for radiative effects on fog and the Earth's surface energy balance, the radiation code RRTMG (Clough et al., 2005) has been recently coupled to PALM, running as an independent single column model for each vertical column of the LES domain. RRTMG calculates the radiative fluxes (shortwave and longwave) for each grid volume while considering profiles of pressure, temperature, humidity, liquid water and the droplet number concentration (n_c). Compared to the precursor study of Maronga and Bosveld (2017), improvements in the microphysics parameterization introduced in the scope of the present study allow a more realistic calculation of the fog's radiation budget, since n_c is now represented as a prognostic

quantity instead of the previously fixed value. This favors an improved calculation of the effective radius, which is given as

$$r_{\text{eff}} = \left(\frac{3 \, q_l \, \rho}{4\pi \, n_c \rho_l} \right)^{\frac{1}{3}} \exp(\log(\sigma_g)^2), \tag{1}$$

where q_l is the liquid water mixing ratio, ρ the air density, ρ_l being density of water and σ_g=1.3 the geometric standard deviation of the droplet distribution. The effective droplet radius is the main interface between the optical properties of the cloud and the
5   radiation model RRTMG. Note, that 3D radiation effects of the cloud are not implemented in this approach, which however could affect the fog development at the lateral edges during formation and dissipation phases when no homogeneous fog layer is present. Radiation calculations traditionally require enormous computational time, the radiation code is called at fixed intervals on the order of 1 min only.

Moreover, PALM's land surface model (LSM) is used to calculate the surface fluxes of sensible and latent heat. The LSM
10 consists of multi-layer soil model, predicting soil temperature and soil moisture, as well as a solver for the energy balance of the Earth's surface using a resistance parameterization. The implementation is based on the ECMWF-IFS land surface parametrization (H-TESSEL) and its adaptation in the DALES model (Heus et al., 2010). A description of the LSM and a validation of the model system for radiation fog is given in Maronga and Bosveld (2017).

2.2   Bulk microphysics

15 As a part of this study, the two-moment microphysics scheme of Seifert and Beheng (2001; 2006) implemented in PALM, which basically only predicts the rain droplet number concentration (n_r) and cloud water mixing (q_r) was extended by prognostic equations for n_c and cloud water mixing ratio (q_c). The scheme of Seifert and Beheng (2001; 2006) is based on the separation of the cloud and rain droplet scale by using a radius threshold of $40\,\mu\text{m}$. This separation is mainly used for parameterizing coagulation processes by assuming different distribution functions for cloud and rain droplets. However, as collision and
20 coalescence are weak in fog due to small average droplet radii, the production of rain droplets is negligible. Consequently, only the number concentration and mixing ratio of droplets (containing all liquid water and thus abbreviated with q_l here) are considered in the following. The budgets of the cloud water mixing ratio and number concentration are given by

$$\frac{\partial q_l}{\partial t} = -\frac{\partial u_i q_l}{\partial x_i} + \left(\frac{\partial q_l}{\partial t} \right)_{\text{activ}} + \left(\frac{\partial q_l}{\partial t} \right)_{\text{cond}} - \left(\frac{\partial q_l}{\partial t} \right)_{\text{auto}} - \left(\frac{\partial q_l}{\partial t} \right)_{\text{accr}} - \left(\frac{\partial q_l}{\partial t} \right)_{\text{sedi}}, \tag{2}$$

$$\frac{\partial n_c}{\partial t} = -\frac{\partial u_i n_c}{\partial x_i} + \left(\frac{\partial n_c}{\partial t} \right)_{\text{activ}} - \left(\frac{\partial n_c}{\partial t} \right)_{\text{evap}} - \left(\frac{\partial n_c}{\partial t} \right)_{\text{auto}} - \left(\frac{\partial n_c}{\partial t} \right)_{\text{accr}} - \left(\frac{\partial n_c}{\partial t} \right)_{\text{sedi}}. \tag{3}$$

25 The terms on the right-hand side represent the decrease or increase by advection, activation, diffusional growth, autoconversion, accretion, and sedimentation (from left to right). Following Ackerman et al. (2009), cloud water sedimentation is parameterized assuming that droplets are having a log-normal distribution and following a Stokes regime. This results in a sedimentation flux of

$$F_{q_l} = k \left(\frac{4}{3} \pi \rho_l n_c \right)^{-2/3} (\rho q_l)^{\frac{5}{3}} \exp(5 \ln^2 \sigma_g), \tag{4}$$

with the parameter $k = 1.2 \cdot 10^8\,\mathrm{m^{-1}s^{-1}}$ (Geoffroy et al., 2010). The main focus of this paper is to study the effect of different microphysical parameterizations of activation and condensation processes on microphysical and macroscopic properties of radiation fog. Those different activation and condensation parameterizations will be discussed in the following.

2.2.1 Activation

It is well known that the aerosol distribution and the activation process are of great importance to the life cycle of fog (e.g. Gultepe et al., 2007). The amount of activated aerosols determines the number concentration of droplets within the fog, which in turn has a significant influence on radiation through optical thickness as well as on sedimentation and consequently influences macroscopic properties of the fog, such as its vertical extension. For these reasons, a sophisticated treatment of the activation process is an essential prerequisite for the simulation of radiation fog. Several parameterizations for bulk microphysics models have been developed to provide a realistic activation model. In this work, three of these activation schemes were compared with each other in order to quantify their influence on the development of a radiation fog event. The schemes considered in this scope are the simple activation scheme of Twomey (1959) which was used, e.g., by Bott and Trautmann (2002) to simulate radiation fog, the scheme of Cohard et al. (1998) (used by e.g. Stolaki et al., 2015; Mazoyer et al., 2017) and the one by Khvorostyanov and Curry (2006). The latter two represent an empirical and analytically extension of Twomeys scheme, respectively. Consequently, these parameterizations are frequently termed Twomey-type parameterizations with the general type of

$$N_{\mathrm{CCN}}(s) = N_0 s^k, \tag{5}$$

where N_{CCN} are the number of activated cloud condensation nuclei (CCN), N_0 and k are parameters depending on the aerosol distribution, and s is the supersaturation. This equation can be solved using several approaches and mathematical complexity levels. In the following, these three schemes and their underlying equations are presented.

1. **Twomey (1959):** The simple power law expression (see Eq. 5) is well known and has been used for decades to estimate the number of activated aerosol for a given air mass in dependence of the supersaturation. A weakness of this approach is that the parameters N_0 and k are usually assumed to be constant and are not directly linked to the microphysical properties. Furthermore, this relationship creates an unbounded number of CCN at high supersaturations.

2. **Cohard et al. (1998):** extended Twomey's power law expression by using a more realistic four-parameter CCN activation spectrum as shaped by the physiochemical properties of the accumulation mode. Although an extension to the multi-modal representation of an aerosol spectrum would be possible, all relevant aerosols that are activated in typical supersaturations within clouds and especially fog are represented in the accumulation mode (Cohard et al., 1998; Stolaki et al., 2015). Following Cohard et al. (1998) and Cohard and Pinty (2000) the activated CCN number concentration is expressed by

$$N_{\mathrm{CCN}}(s) = C s^k \cdot F\left(\mu, \frac{k}{2}, \frac{k}{2} + 1; \beta s^2\right) \tag{6}$$

while C is proportional to the total number concentration of CCN that is activated when supersaturation s tends to infinity. Parameters k, μ, and β are adjustable shape parameters associated with the characteristics of the aerosol size spectrum such as geometric mean radius and the geometric standard deviation as well as with chemical composition and solubility of the aerosols. Thus, in contrast to a simple Twomey approach, the influence of physiochemical properties of the aerosol spectrum are taken into account.

3. **Khvorostyanov and Curry (2006):** have found an analytical solution to express the activation spectrum using Koehler theory. Therein, it is assumed that the dry aerosol spectrum follows a log-normal size distribution of aerosol f_d:

$$f_d = \frac{dN_a}{dr_d} = \frac{N_t}{\sqrt{2\pi}\ln\sigma_d r_d} \exp\left[-\frac{\ln^2(r_d/r_{d0})}{2\ln^2\sigma_d} \right]. \tag{7}$$

Here, r_d is the dry aerosol radius, N_t the total number of aerosols, σ_d is the dispersion of the dry aerosol spectrum, and r_{d0} is the mean radius of the dry particles. The number of activated CCN as a function of supersaturation s is then given by

$$N_{CCN}(s) = \frac{N_t}{2}[1 - \text{erf}(u)]; \qquad u = \frac{\ln(s_0/s)}{\sqrt{2}\ln\sigma_s}, \tag{8}$$

where erf is the Gaussian error function, and

$$s_0 = r_{d0}^{-(1+\beta)}\left(\frac{4A^3}{27b}\right)^{1/2}, \qquad \sigma_s = \sigma_d^{1+\beta}. \tag{9}$$

In this case, A is the Kelvin parameter and b and β depend on the chemical composition and physical properties of the soluble part of the dry aerosol.

Since prognostic equations were neither considered for the aerosols nor their sources and sinks, a fixed aerosol background concentration was prescribed by setting parameters N_0, C and N_t for the three activation schemes. The different nomenclature of the aerosol background concentration is based on the nomenclature used in the original literature.

The activation rate is then calculated as

$$\left(\frac{\partial n_c}{\partial t}\right)_{activ} = \max\left(\frac{N_{CCN} - n_c}{\Delta t}, 0\right), \tag{10}$$

where n_c is the number of previously activated aerosols that are assumed to be equal to the number of pre-existing droplets and Δt is the length of the model time step. It should be noted that this method does not represent the reduction of CCN. However, this error can be neglected since processes as aerosol washout and dry deposition are of minor importance for radiation fog. For all activation schemes it is assumed that every activated CCN becomes a droplet with an initial radius of 1 µm. This results in a change of liquid water, which is considered by the condensation scheme and is described in the next section. Furthermore, we performed a sensitivity study with initial radii of 0.5 µm to 2 µm, which showed that the choice of the initial radius had no impact on the results (not shown). This is consistent with the findings of Khairoutdinov and Kogan (2000) and Morrison and Grabowski (2007).

2.2.2 Condensation

The representation of diffusional growth, evaporation, and calculating the underlying supersaturation is one of the fundamental tasks of cloud physics. Three different methods have been evaluated and widely discussed in the scientific community. Namely these are the saturation adjustment scheme, the simple explicit scheme, where the supersaturation is derived by the prognostic fields of temperature and water vapor, and a prognostic calculation method of the supersaturation following (e.g. Clark, 1973; Morrison and Grabowski, 2007; Lebo et al., 2012). Basically, the supersaturation is given by $s = q_v/q_s - 1$, while the absolute supersaturation (or water vapor surplus) is defined as $\delta = q_v - q_s$, where q_v is the water vapor mixing ratio and q_s is the saturation mixing ratio. In the following, these three methods are reviewed briefly.

1. **Saturation adjustment:** In many microphysical models, a saturation adjustment scheme is applied. The basic idea of this scheme is that all supersaturation is removed within one model time step and supersaturations are thus neglected; and thus potentially leads to excessive condensation. Despite the many years of application of this scheme, its influence on microphysical processes is discussed controversially in the community (e.g. Morrison and Grabowski, 2008; Thouron et al., 2012; Lebo et al., 2012). Saturation adjustment might hence especially be a source of error in fog simulations where very small time steps are used due to small grid spacings as outlined earlier. Using the saturation adjustment scheme, q_l represents a diagnostic value calculated by means of

$$q_l = \max(0, q - q_r - q_s), \tag{11}$$

   where q is the total water mixing ratio. The saturation mixing ratio, which is a function of temperature, is approximated in a first step by

$$q_s(T_l) = \frac{R_d}{R_v} \frac{e_s(T_l)}{p - e_s(T_l)}, \tag{12}$$

   where T_l is the liquid water temperature and p is pressure. The individual gas constants for dry air and water vapor are denoted R_d and R_v, respectively. For the saturation vapor pressure e_s an empirical relationship of Bougeault (1981) is used. In a second step q_s is corrected using a first-order Taylor series expansion of q_s:

$$q_s(T) = q_s(T_l)\frac{1 + \beta q}{1 + \beta q_s(T_l)}, \tag{13}$$

   with

$$\beta = \frac{L_v}{R_v c_p T_l^2}, \tag{14}$$

   where c_p is the specific heat of dry air and L_v is the latent heat of vaporization. As aforementioned, in each model time step, all supersaturation is converted into liquid water or, in subsaturated regions, the liquid water is reduced until saturation. Therefore, for using the saturation adjustment scheme and a calculation of aerosol activation, the supersaturation must be estimated. For that, using the activation scheme of Cohard et al. (1998) the supersaturation is estimated following Thouron et al. (e.g. 2012); Mazoyer et al. (e.g. 2017); Zhang et al. (e.g. 2014) and directly translated into a droplet

number concentration by

$$s^{k+2} \cdot F\left(\mu, k/2, k/2+1, -\beta s\right) = \frac{\left(\phi_1 w + \phi_3 \frac{dT}{dt}\big|_{\text{rad}}\right)^{3/2}}{2kC\pi\rho_l\phi_2 B(k/2, 3/2)}, \tag{15}$$

where ϕ_1, ϕ_2 and ϕ_3 are functions of temperature and pressure and given in Cohard et al. (1998) and Zhang et al. (2014). w is the vertical velocity and B the beta function.

5 2. **Explicit supersaturation calculation:** Supersaturation is calculated explicitly from q_v and temperature T (from which q_s can be derived). However, since it is assumed that the supersaturation is kept constant during one model time step, the explicit approach requires a very small model time step of

$$\Delta t \le 2\tau, \tag{16}$$

due to stability reasons (Árnason and Brown Jr, 1971). Here, τ is the supersaturation relaxation time which is approxi-
10 mated by

$$\tau \approx (4\pi D n_c \langle r \rangle)^{-1}, \tag{17}$$

where $\langle r \rangle$ is the average droplet radius, and D the diffusivity of water vapor in air. Due to the low dynamic time step in the present study imposed by the Courant-Friedrichs-Lewy criterion (on the order of 0.1 s), however, the condensation time criterion is fulfilled, and no additional reduction of the time step is needed. The rate of cloud water change due to
15 condensation or evaporation is given by

$$\left(\frac{\partial q_l}{\partial t}\right)_{\text{cond}} = \frac{4\pi G(T,p)\rho_w}{\rho_a} s \int_0^\infty r f(r) dr \tag{18}$$

$$= \frac{4\pi G(T,p)\rho_w}{\rho_a} s r_c \tag{19}$$

where r_c is the integral radius and $G = \frac{1}{F_K+F_D}$ included the thermal conduction and the diffusion of water vapor (Khairoutdinov and Kogan, 2000). The density ratio of liquid water and the solute is given by ρ_w/ρ_a. Using such a
20 small time step allows the use of a diagnostic approach for the supersaturation calculation.

3. **Prognostic supersaturation:** The prognostic/ semi-analytic approach, which was first introduced by Clark (1973), includes an additional prognostic equation for the absolute supersaturation. Even though this requires further computational costs for solving one more prognostic equation, it mitigates the problem of spurious cloud-edge supersaturations and prevent inaccurate supersaturation caused by small errors in the advection of heat and moisture (Morrison and Grabowski,
25 2007; Thouron et al., 2012).

The temporal change of the absolute supersaturation is given by

$$\frac{\partial \delta}{\partial t} - \frac{1}{\rho}\nabla \cdot (u\,\rho\delta) = A - \frac{\delta}{\tau}, \tag{20}$$

with A described by

$$A = -q_{\mathrm{s}} \frac{\rho g w}{p - e_{\mathrm{s}}} - \frac{dq_{\mathrm{s}}}{dT} \cdot \left[\frac{g w}{c_{\mathrm{p}}} + \left(\frac{dT}{dt} \right)_{\mathrm{rad}} \right], \tag{21}$$

with g being gravitational acceleration. The supersaturation relaxation time is given in Eq. 17. The second term on the left hand side of Eq. 20 describes the change of the absolute supersaturation due to advection, while the right hand side considers effects for δ to changes in pressure, adiabatic compression/expansion, and radiative effects (from left to right). By doing so, the predicted supersaturation is used for determining the number of activated droplets as well as the condensation and evaporation processes.

3 Case description and model setup

The simulations performed in the present study are based on an observed deep fog event during the night from 22 to 23 March 2011 at the Cabauw Experimental Site for Atmospheric Research (CESAR). The fog case is described in detail in Boers et al. (2013) and was used as validation case for PALM in Maronga and Bosveld (2017). The CESAR site is dominated by rural grassland landscape and, although it is relatively close to the sea, there are typically continental aerosol conditions characterized by agricultural processes (Mensah et al., 2012).

The fog initially formed at midnight (as a thin near-surface layer), induced by radiative cooling, which also produced a strong inversion with a temperature gradient of 6 K between the surface and the 200 m tower-level. In the following the fog layer began to develop: At 0300 UTC the fog had a vertical extension of less than 20 m, then deepened rapidly to 80 m, and reaching 140 m depth at 0600 UTC. At 0300 UTC, also the visibility had reduced to less than 100 m. After sunset (around 0545 UTC) a further invigoration close to the ground was suppressed and after 0800 UTC the fog starts quickly evaporate due to direct solar heating of the surface. For details, see Boers et al. (2013).

The model was initialized as described in the precursor study of Maronga and Bosveld (2017). Profiles of temperature and humidity (see Fig. 1) were derived from the CESAR 200 m-tower and used as initial profiles in PALM. A geostrophic wind of $5.5 \, \mathrm{m \, s^{-1}}$ was prescribed based on the observed value at Cabauw at 0000 UTC.

The land surface model was initialized with short grassland as surface type and four soil model layers at the depths of 0.07 m, 0.28 m, 1.0 m and 2.89 m. The measured surface layer temperatures were interpolated to the respective levels, resulting in temperatures of 279.54, 279.60, 279.16, and 279.16 K for soil layers one to four, respectively. Furthermore, the initial soil moisture was set to the value at field capacity ($0.491 \, \mathrm{m^3 m^{-3}}$), which reflects the very wet soil and low water table in the Cabauw area. The heat conductivity was set to $\Lambda = 4$, based on the radiation and energy balance observed at 0000 UTC at Cabauw. Moreover, the roughness length for momentum was prescribed to 0.15 m. Note that Maronga and Bosveld (2017) discussed that this value appears to be a little high given the season and wind direction. This does not play an important role for the present study, however, as we will not focus on direct comparison against observational data from Cabauw.

All simulations start at 0000 UTC, before fog formation, and end at 1015 UTC on the next morning after the fog layer has fully dissipated. Precursor runs are conducted for additional 25 min using the initial state at 0000 UTC, but without radiation
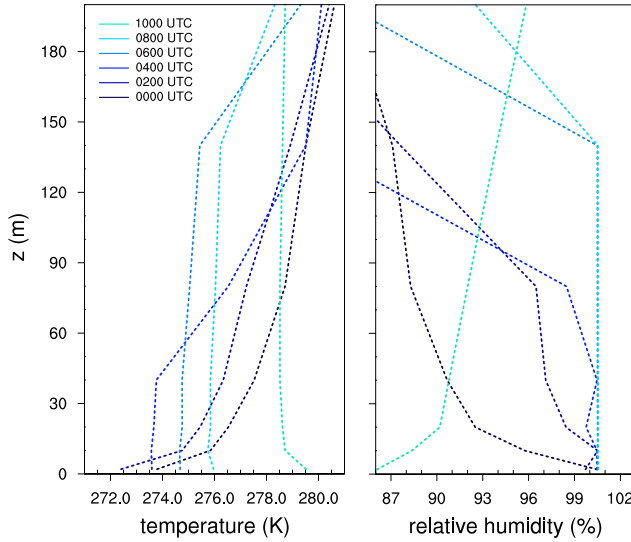
Figure 1. Profiles of potential temperature and relative humidity at different times as observed at Cabauw.

scheme and LSM in order to allow the development of turbulence in model without introducing feedback during that time (see Maronga and Bosveld, 2017).

Based on sensitivity studies of Maronga and Bosveld (2017), a grid spacing of $\Delta = 1\,\mathrm{m}$ was adopted for all simulations, with a model domain size of 768 x 768 x 384 grid points in x-, y-, and z-direction, respectively. A sponge layer was used starting at
5   a height of 344 m in order to prevent gravity waves from being reflected at the top boundary of the model.

Tab.1 gives on overview over the simulation cases. All cases were initialized with (identical) continental aerosol conditions. Case SAT represents a reference run with no activation scheme and thus a prescribed constant value of $n_\mathrm{c} = 150\,\mathrm{cm}^{-3}$ (estimated from simulations of Boers et al. (2013)). This case represents a similar setup to the one described in Maronga and Bosveld (2017). Condensation processes were here treated with the saturation adjustment scheme (Seifert et al., 2006).
10   In order to evaluate the influence of saturation adjustment on the development of radiation fog, identical assumptions were made in case EXP and PRG, except that diffusion growth was calculated with the explicit and prognostic method (see section 2.2.2), respectively. Cases N1EXP-N3EXP used the activation schemes described in chapter 2.2.1. To ensure comparability between the different schemes, all of them were initialized with a continental aerosol background described in Cohard et al. (1998), which is characterized by an aerosol with the chemical composition of ammonium sulfate $[(\mathrm{NH}_4)_2\mathrm{SO}_4]$, a back-
15   ground aerosol concentration of $842\,\mathrm{cm}^{-3}$, a mean dry aerosol radius of $r_\mathrm{d0} = 0.0218\,\mathrm{\mu m}$, and a dispersion parameter of the dry aerosol spectrum of $\sigma_\mathrm{d} = 3.19$. For the Twomey activation scheme this results in $N_0 = 842\,\mathrm{cm}^{-3}$ and $k = 0.8$ which is a typical value for the exponent for continental air masses (e.g. Pruppacher and Klett, 1997, pages 289 et seq.). The Twomey activation scheme does not allow for taking aerosol properties into account. In contrast, the activation scheme of Cohard et al. (1998) requires the parameters C, k, β and μ to be derived from the aerosol properties. Here, values of $C = 2.1986 \cdot 10^6\,\mathrm{cm}^{-3}$,
20   $k = 3.251$, $\beta = 621.689$ and $\mu = 2.589$ were used as described in Cohard and Pinty (2000). Finally, the activation scheme of

Table 1. Overview of conducted simulations. The droplet number concentration n_c is only prescribed for simulations without activation scheme. In the simulations N1EXP-N3EXP n_c is a prognostic quantity and thus variable in time and space. The aerosol background concentration is abbreviated with $N_{a,tot}$, and used to initialize the activation schemes. Note for the scheme of (Cohard et al., 1998) a conversion to the parameter C must be applied, while for both other activation schemes this value is directly used to prescribe N_0 and N_t, respectively.

#	Simulation	Activation scheme	n_c [cm^{-3}]	$N_{a,tot}$ [cm^{-3}]	Condensation scheme
1	SAT	none	150	none	saturation adjustment
2	EXP	none	150	none	explicit
3	PRG	none	150	none	prognostic
4	N1EXP	Twomey (1959)	not fixed	842	explicit
5	N2EXP	Cohard et al. (1998)	not fixed	842	explicit
6	N3EXP	Khvorostyanov and Curry (2006)	not fixed	842	explicit
7	N2SAT	Cohard et al. (1998)	not fixed	842	saturation adjustment
8	N2PRG	Cohard et al. (1998)	not fixed	842	prognostic

Khvorostyanov and Curry (2006) can directly consider the aerosol properties, which are prescribed as aforementioned. Since changing other microphysical properties (such as mean geometric radius, chemical composition, or dispersion of dry aerosol spectrum) will have a similar effect to the physical outcomes as the variation of the aerosol concentration (because only cloud number concentration is affected), further simulation cases were omitted. Moreover, for investigating the impact of the super-saturation calculation on CCN activation (see section 4.4) the simulation N2SAT, N2EXP and N2PRG were compared to each other. In all three cases the activation scheme of Cohard et al. (1998) is used.

4 Results

4.1 General fog life cycle and macrostructure

The reference case SAT is conducted with a constant droplet number concentration of $n_c = 150\,\mathrm{cm}^{-3}$. The deepening of the fog layer can be seen in Fig. 2, which shows the profiles of the potential temperature, relative humidity and liquid water mixing ratio at different times.

The fog onset is at 0055 UTC, defined by a visibility below 1000 m and a relative humidity of 100%. In the following the fog layer deepens and extends to a top of approximately 20 m at 0200 UTC. However, at this point the stratification of the layer is still stable with a temperature gradient of 6 K between the surface and the fog top. The persistent radiative cooling of the surface and the fog layer leads to a further vertical development of the fog, which is accompanied with a regime transition from stable to convective conditions within the fog layer (see Fig. 2a). This starts as soon as the fog layer begins to become optically thick (at 0330 UTC), and when radiative cooling at the fog top becomes the dominant process, creating a top-down convective boundary layer. The highest liquid water mixing ratio of $q_l = 0.41\,\mathrm{g\,kg}^{-1}$ is achieved at 0600 UTC at a height of
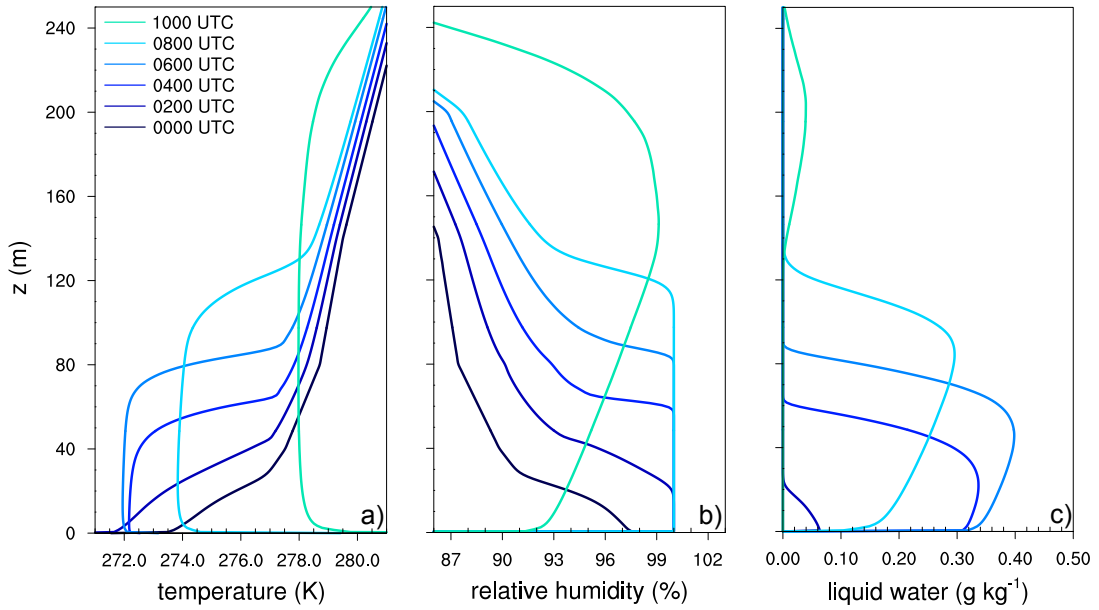
Figure 2. Profiles of potential temperature (a), relative humidity (b) and liquid water mixing ratio (c) at different times for the reference case REF.

60 m (see Fig. 2c), while the the fog layer in total reaches the maximum one hour later at 0700 UTC. The lifting of the fog, which is defined by a non-cloudy near-surface layer ($q_l \leq 0.01\,\mathrm{g\,kg^{-1}}$), occurs at 0845 UTC. At 1130 UTC the fog is completely dissipated.

4.2 Influence of different supersaturation parameterizations on diffusional growth

In this section we discuss the error introduced by using saturation adjustment for simulating radiation fog. For this, we compare three simulations with identical setup (cases SAT, EXP, and PRG), differs only in the way how supersaturation is calculated and consequently the amount of condensed or evaporated liquid water. To isolate this effect, activation is neglected in all cases and n_c is set to a constant value of $150\,\mathrm{cm^{-3}}$. The effect on different supersaturations driving the diabatic process of activation is discussed in section 4.4. Due to the small grid spacing of 1 m used in our simulations, the time step is in the order of 10^{-1} s, which is more than one order of magnitude smaller than the allowed values of 2-5 s for assuming saturation adjustment (Thouron et al., 2012). The present case hence is an ideal environment evaluating the error introduced by using saturation adjustment and by keeping all other parameters fixed.

Figure 3 shows time series of the horizontally-averaged saturation (supersaturation) for SAT, EXP and PRG case. In all cases saturation occurs simultaneously around 0120 UTC. In case SAT, relative humidity does not exceed 100% due to its limitation by saturation adjustment, while in case EXP and PRG average supersaturations of 0.05% in 2 m occur, which corresponds to typical values within fog (Hammer et al., 2014; Mazoyer et al., 2017; Boutle et al., 2018).
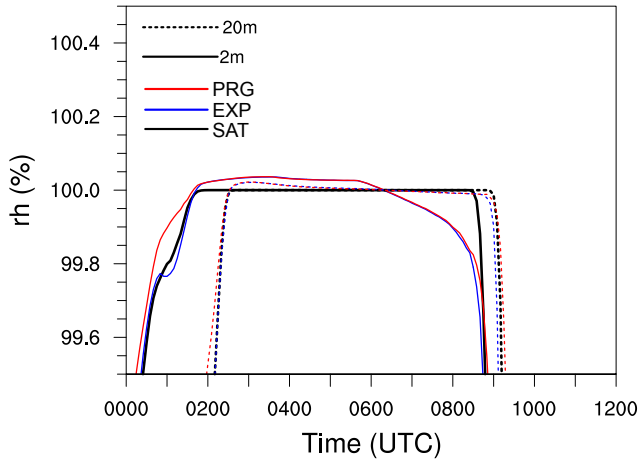
Figure 3. Time series of horizontal-averaged relative humidity/supersaturation at height levels of 2 m (dotted) and 20 m (dashed) for different methods in treating the supersaturation calculation.
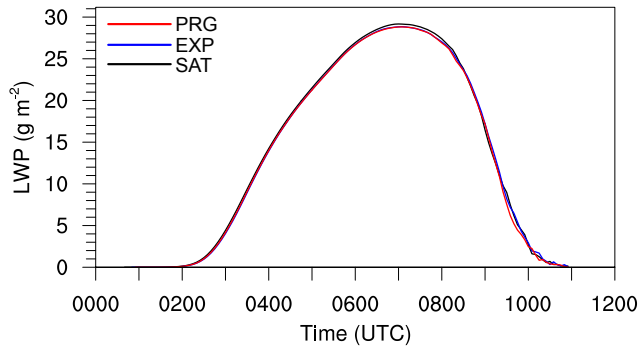
Figure 4. Time series of liquid water path (LWP) for cases using saturation adjustment, the explicit approach and a prognostic method for the diffusional growth.

For case EXP and PRG starting from 0615 UTC (in 2 m height) and 0715 UTC (in 20 m height), supersaturations are removed and the air becomes subsaturated (on average). This is in contrast with case SAT, where the saturation adjustment approach keeps the relative humidity at 100% as long as liquid water is present (i.e. until the fog has dissipated). Around 0600 UTC, which is shortly after sunrise, relative humidity drops rapidly as a direct consequence of direct solar heating of the surface and the near-surface air, preventing further supersaturation at these heights. While we cannot clearly identify the lifting of the fog in case EXP and PRG (due to the limited humidity range displayed), we note that for case SAT we can identify lifting times as a decrease of relative humidity around 0845 UTC at 2 m height and around 0910 UTC at 20 m height.

Beside this inherent difference in relative humidity, the general time marks (formation, lifting, dissipation, defined as in Maronga and Bosveld (2017)) of the fog layer are identical for cases SAT, EXP and PRG.
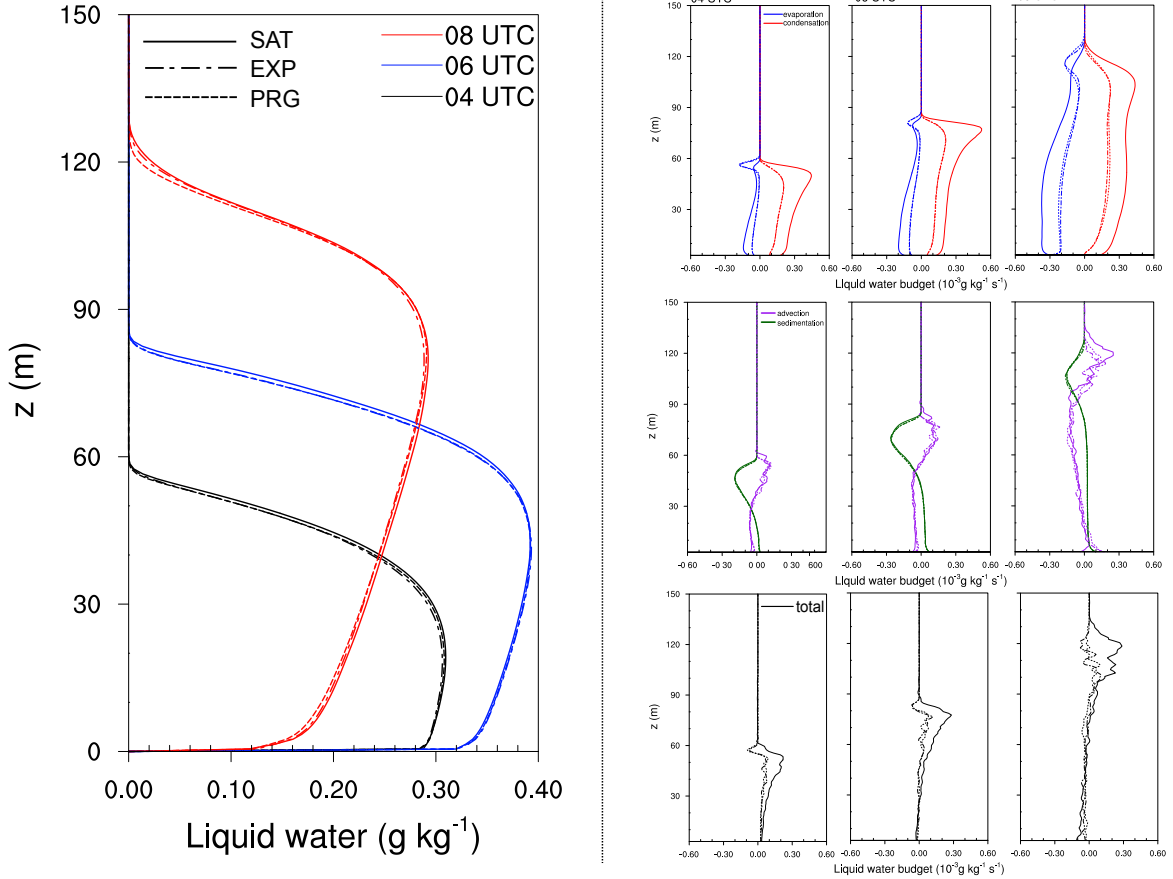
Figure 5. Instantaneous horizontally averaged profiles for the liquid water mixing ratio (left) for 0400 UTC, 0600 UTC and 0800 UTC and budgets for q_l tendencies (right, upper row: condensation and evaporation, middle row: sedimentation and advection and lower row: total tendency) for 0400 UTC, 0600 UTC and 0800 UTC for the simulations SAT, EXP and PRG.

Figure 4 shows the liquid water path (LWP) for all cases. Differences in the LWP appear between 0400 UTC and 1100 UTC and do not exceed 1% (lower values for cases EXP and PRG), indicating that the choice of the condensation scheme does not affect the total water content of the simulated fog layer.

4.2.1 Budget of liquid water

5 Fig. 5 shows profiles for the liquid water mixing ratio (left) as well as the liquid water budgets at 0400 UTC, 0600 UTC and 0800 UTC for cases SAT, EXP and PRG. These times represent different stages of the fog development: deepening, mature phase, and mature phase development after sunrise, respectively. Figure 5a confirms that especially at the top of the fog, when it becomes radiative active, the liquid water is slightly higher in the case of saturation adjustment, but in general the differences between the runs are negligible. Figures 5 (right) show a clear trend: On the one hand the sedimentation and advection rates
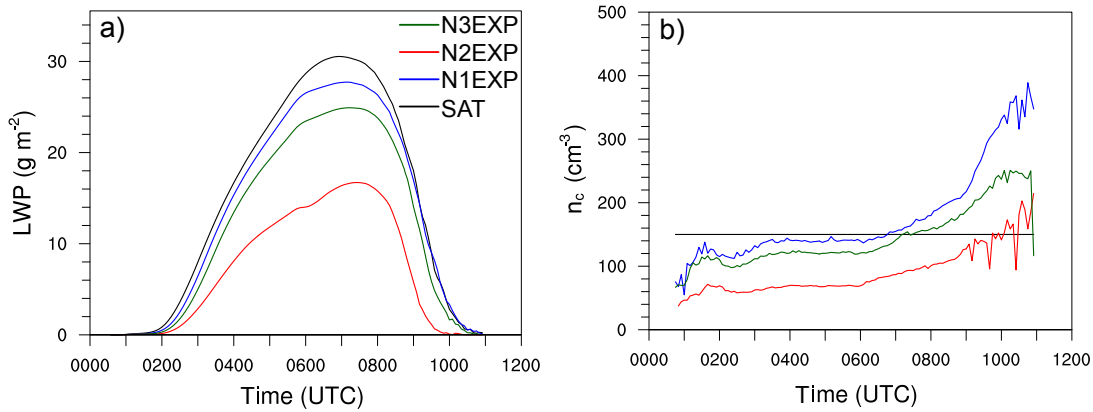
Figure 6. Time series of LWP and n_c (as a horizontal and vertical average of the fog layer) for the reference and N1EXP-N3EXP case.

are almost identical for all cases at all times. On the other hand, clear differences can be observed in the production rate for condensation and the dissipation rate due to evaporation. In the case of saturation adjustment, these rates are almost twice as high (in absolute sense) as for the cases EXP and PRG over the entire height of the fog layer. This finding can be attributed to the fact that saturation adjustment is assuming the highest possible values for condensation. This in turn also affects the

5 evaporation rates, which are counteracting the production by excessive condensation. The net effect, however, is small (c.f. Fig. 4).

It can be summarized that, although the assumptions of saturation adjustment are not valid for the simulation of fog when using a very small time step, the mean liquid water content is not changed by more than 1% and the general fog structure is not altered. This is probably due to the very small supersaturation that is not strong enough to generate a significant change

10 in the effective droplet radius, and which could lead to stronger sedimentation or higher radiative cooling rates. But as the different methods calculating supersaturation are not strong enough to create any noteworthy differences in condensational growth by using 1-moment microphysics (keeping the droplet number concentration constant), the impact of these differences for activation might be crucial and is discussed in section 4.4.

4.3 Comparison of different activation parameterizations

15 In numerous previous studies, the influence of aerosols and the activation process on the life cycle of fog was investigated (e.g. Bott, 1991; Stolaki et al., 2015; Maalick et al., 2016; Zhang et al., 2014; Boutle et al., 2018). Although all three activation schemes outlined in section 2.2.1 are comparable power law parameterizations that are initialized with identical aerosol spectra, the influence on fog is still unknown, since changes in n_c due to different activation schemes have considerable effects on the life cycle of fog and thus also small differences in n_c might have a significant feedback.

20 Furthermore, n_c, as a function of time and averaged over the fog volume, is shown in Fig. 6b for the reference case and cases N1EXP-N3EXP, representing runs with the three different aerosol activation parameterization schemes (see Tab.1). The quantitative differences in the number of activated aerosol by using the different activation schemes is explained by a slightly
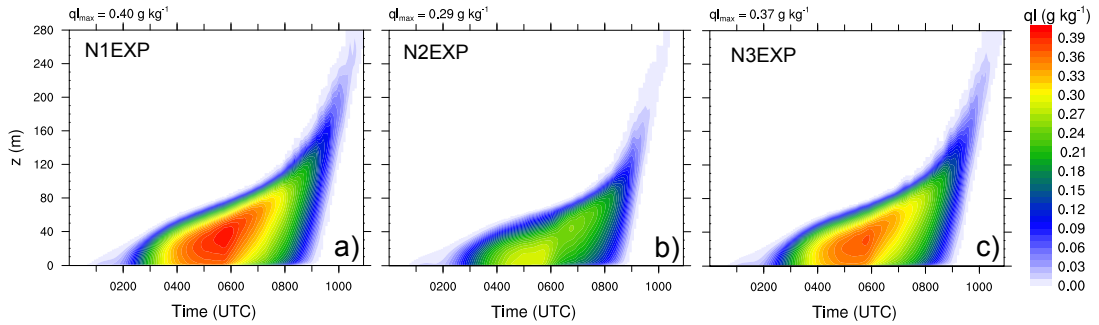
Figure 7. Height-time cross sections for the liquid water mixing ratio for N1EXP-N3EXP.
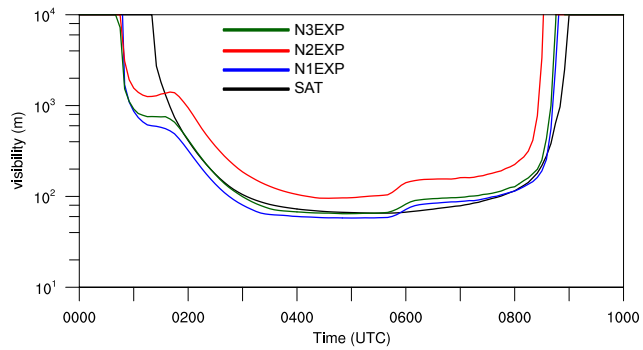
Figure 8. Time series of simulated visibility in 2 m height.

different activation spectrum (see Appendix, Fig. A1). In principle, a similar qualitative development of n_c can be observed. While n_c increases during fog formation, it remains nearly constant during the mature phase of the fog. This can be explained by a constant longwave cooling at the fog top, producing similar supersaturations. As soon as the sun rises and the fog layers start to lift, all cases show a strong increase in n_c. This increase can be explained by stronger supersaturations induced by thermal updrafts in the developing surface-driven convective boundary layer due to surface heating by solar radiation. Moreover, we

5   note that while the qualitative course of n_c is similar for all cases, the choice of the activation algorithm has an impact on number of activated aerosols and thus on the strength of the fog-layer (see Fig. 7). This is due to the radiation effect of the droplets. The number of droplets to which a certain amount of liquid water is distributed plays an important role: the larger the number of droplets, the larger is the radiation-effective surface and the higher also the optical thickness. As a result, on the one

10   hand, the cooling rate from a fog with many small droplets is increased, allowing more water vapor to condense and the fog to grow stronger. On the other hand, however, sedimentation also depends on the droplet radius and plays a major role that will be discussed later. Time series of the LWP for the reference run and the three different cases are shown in Fig. 6a. The highest LWP occurs for the reference run which also shows the highest n_c during the formation and mature phase in comparison with the other simulations. Also for the cases N1EXP-N3EXP a linear relationship between LWP and n_c can be found: A higher n_c

15   leads to higher LWP.

In Fig. 8 the simulated visibility for the cases N1EXP-N3EXP in 2 m height as well as the observed value is shown. Visibility is calculated from the LES data following following Gultepe et al. (2006) as

$$vis = \frac{1002}{(n_c \, \rho \, q_l)^{0.6473}}, \tag{22}$$

(with n_c and q_l given in units of cm^{-3} and gm^{-3}, respectively). Hence, the visibility is significantly affected by the droplet
5 number concentration and the liquid water content. In contrast to the former part of the study, where the droplet number concentration is a constant value, the analysis of the visibility is interesting here as the activation schemes significantly alter n_c and q_l for the different cases within the fog layer.

We note that visibility follows the same general temporal developed in all simulations with a rapid decrease during fog formation, deepening, and dissipation; with minimum values around 100 m (which is similar to the observations). We also see
10 noteworthy differences, particularly shortly before 0200 UTC (before fog deepening) at around 0545 (shortly after sunrise). For both time marks, case N1EXP - N3EXP display sudden increases in visibility, due to an fast decrease of n_c in 2 m height; and which are not reproduced by case SAT, as n_c is fixed value in this case. Also, the time marks of formation and dissipation vary. For cases N1EXP - N3EXP the formation time is significantly advanced compared to case SAT, while dissipation time only shows a small tendency towards earlier times, at least for N1EXP and N3EXP. Case N2EXP displays a different behavior,
15 with a later fog formation and higher visibility and accordingly earlier dissipation time. This is in line with the findings discussed above (i.e. a much weaker fog layer that, as a direct consequence, can dissipate much faster). Otherwise, all cases display almost identical visibility as soon as the fog has deepened.

4.3.1   Budgets of liquid water and droplet number concentration

Figure 9a shows the profiles of the liquid water mixing ratio at 0400 UTC, 0600 UTC, and 0800 UTC. The maximum q_l in the
20 fog layer is reached at approximately 0600 UTC at a height of 60 m. Afterwards a further vertical growth of the fog can be observed, where no further increase in liquid water takes places as a result of larger vertical extent of the mixing layer and due to rising temperatures after sunrise (see Fig. 5a). Moreover, Fig. 9b,c show the liquid water budget during the mature phase of the fog at 0600 UTC, when the fog was fully developed. Almost all three cases show identical values for condensation rates (see Fig. 9b) in the lowest part of the fog layer, with values being in the same order as the evaporation rates, so that
25 the net gain in this region appears to be small. However, the N2EXP case (with the lowest n_c) exhibits a generally lower absolute evaporation rate compared to both other cases, which can be attributed to the slightly higher mean values of the relative humidity (not shown) than in N1EXP and N3EXP. In the upper part of the fog layer, higher values of the condensation rate are observed (especially for N1EXP and N3EXP) with a concurrent decrease in evaporation rates, leading to differently strong deepening of the fog layer. At a height of approximately 80 m a maximum of the evaporation rates can be observed,
30 representing the presence of subsaturated regions in this height and the top of the fog. Larger differences can be observed in the sedimentation rates: First and foremost the sedimentation is proportional to the liquid water mixing ratio (see also Eq. 4). However, the strength of sedimentation also depends on the mean radius of the droplets, which increases with decreasing number of activated drops. Here, a lower n_c for a given amount of liquid water leads to a higher mean radius, compared to

Table 2. Table of fog's life cycle time marks.

Simulation	Onset	Maximum	Lifting	Dissipation
N1EXP	0025 UTC	0510 UTC	0810 UTC	1005 UTC
N2EXP	0050 UTC	0425 UTC	0755 UTC	0910 UTC
N3EXP	0025 UTC	0515 UTC	0810 UTC	0950 UTC

a higher n_c where the same amount of water is distributed to more drops, decreasing the mean radius. Integrated over height all three cases exhibit approximately the same sedimentation rates. Therefore, case N2EXP suffers the most from the loss of liquid water due to sedimentation (in relative terms). Moreover, Fig. 9c shows that sedimentation partially counteracts the gains caused by condensation at the upper edge of the fog. All in all it can be summarized that all shown processes affect

5   the net change of the liquid water mixing ratio. However, in the mature phase sedimentation plays a key role, showing the highest values for the individual tendencies. As a result liquid water is slowly and constantly removed from the fog layer. These findings are in good agreement with investigations by Bott (1991). The sum of all tendencies, which is shown in Fig. 9d, is the height-dependent change of the liquid water. Also here it can be seen that in the lower 50 m the net tendency is negative, while in higher levels we observe a positive tendency, so that the fog continues growing vertically, while the liquid

10   water content within the fog layer decreases.

Figure 10a shows profiles of n_c at 0400 UTC, 0600 UTC and 0800 UTC. We note that the profiles of the different cases differ quantitatively but not qualitatively. The stage of the fog can thus be identified in the profiles for all cases: At 0400 UTC highest supersaturations occur close to the ground due to cooling of the surface and near-surface air, leading to high activation rates and therefore high n_c near the surface. At 0600 UTC a well-mixed layer has developed that is driven by the radiative cooling

15   from the fog top. While the turbulent mixing leads to a vertical well-mixed n_c, we note the maximum at the top, where the radiative cooling induces immense aerosol activation. This is also displayed in the budget of the n_c (see Fig. 10b,c), where the instantaneous rates for 0600 UTC are shown. Here, we see clearly that aerosol activation at the top of the fog layer is the dominant process in the mature phase of the fog, while activation near the surface is relatively unimportant. Also, we see that both, advection and sedimentation are much less important than activation. Finally, we note that evaporation of droplets, though

20   small in magnitude, occurs at the fog top, reflecting updrafts of foggy air penetrating the subsaturated air aloft where droplets then evaporate.

The effect of the different activation schemes on the time of the fog life cycle is summarized in Tab. 2. While N1EXP and N3EXP have similar time marks, N2EXP stands out and show an delayed onset by 25 min, while the maximum liquid water mixing ratio is reached 45 min earlier, than in the other cases. Also lifting and dissipation are affected and occurred 15 min and

25   40 min (with respect to simulation N3EXP) earlier. This is due to a lesser absolute liquid water mixing ratio which evaporates faster by the incoming solar radiation. Therefore, it can be concluded that the use of different activation schemes (if they change the droplet number concentration) has an effect on the time marks on the life cycle as well as on the fog height and the amount of liquid water within the fog layer.
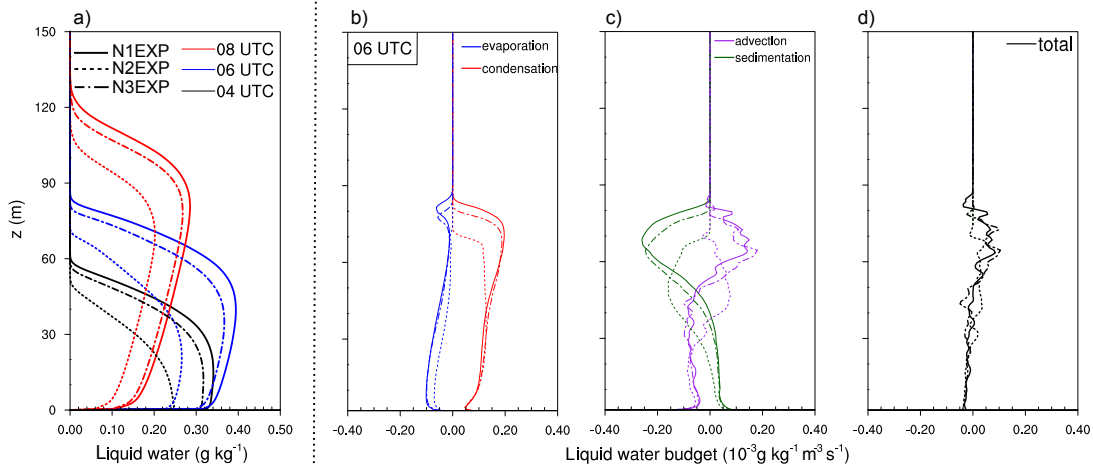
Figure 9. Profiles (instantaneously and horizontally averaged) of liquid water mixing ratio at 0400 UTC, 0600 UTC and 0800 UTC and profiles of explicit liquid water budget terms at 0600 UTC.
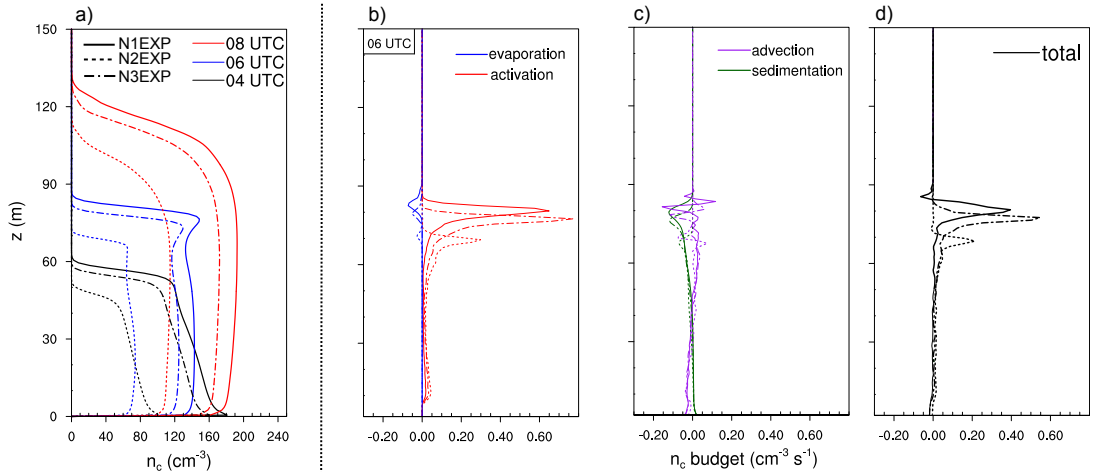
Figure 10. Profiles (instantaneously and horizontally averaged) of n_c at 0400 UTC, 0600 UTC and 0800 UTC and profiles of explicit n_c budget terms at 0600 UTC.

4.4 Impact of supersaturation calculation on CCN activation

The impact of different methods modelling supersaturation on the CCN activation for a radiation fog event is investigated following Lebo et al. (e.g. 2012); Thouron et al. (e.g. 2012). Figure 11 shows the LWP for simulations applying the activation scheme of Cohard et al. (1998) and using saturation adjustment (N2SAT), the explicit scheme (N2EXP) and a prognostic
5   scheme (N2PRG) for calculating supersaturations. It can be seen that the prognostic approach and explicit methods produces very similar values for the LWP. However, in case of saturation adjustment the LWP is nearly 70% higher than for the other
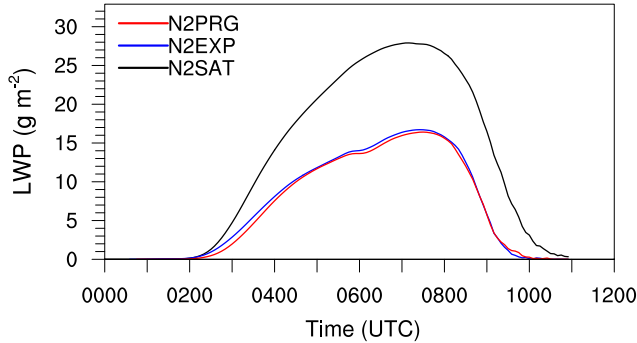
Figure 11. Time series of LWP for simulations using saturation adjustment (N2SAT, black), the explicit scheme (N2EXP, blue) and the prognostic method (N2PRG, red). All cases uses the activation scheme of Cohard et al. (1998).

schemes. In Fig. 12 profiles of the liquid water mixing ratio (left) and droplet number concentration (right) are shown. Here, the number concentration in case N2EXP exhibits slightly higher values as N2PRG, but are both at approximately $100\,\mathrm{cm}^{-3}$ at 0600 UTC. In contrast, in simulation N2SAT a number concentration of $150\,\mathrm{cm}^{-3}$ is observed. Those differences are explained by the different methods for calculating the supersaturation, since activation is the main process altering the droplet number

5 concentration (all other terms of Eq. 3 are less important as shown in Fig. 10). Due to that one can implicitly derive from the droplet number concentration that the prognosed and diagnosed values for the supersaturation using the explicit method and the prognostic method are quite similar. As saturation adjustment removes all supersaturation during one time step, a method for approximating the supersaturation is used (see Eq. 15). By that, the case N2SAT produces a droplet number concentration of $150\,\mathrm{cm}^{-3}$ at 0600 UTC, which is about 50% higher in comparision to N2EXP and N2PRG. However, these differences between

10 N2SAT and N2EXP/N2PRG are in good agreement with the found values of Thouron et al. (2012) for a stratocumulus case (see their Fig. 2) where the number concentration of the explicit and prognostic method were also quite similar and the case with saturation adjustment overestimates the supersaturation and therefore the droplet number concentration. As outlined in the section before, the number concentration has a crucial impact on the LWP as well as on the times of lifting and dissipation of the fog.

15 ### 4.4.1 Grid spacing sensitivity study

To evaluate the effect of grid spacing with different methods for calculating the supersaturation on CCN activation we repeated cases N2SAT, N2EXP and N2PRG each with two coarser grid spacings of 2 m and 4 m. The general effect of the grid spacing to the temporal development and structure of radiation fog is discussed in detail in Maronga and Bosveld (2017). In this section, we will thus focus only on relative changes in LWP due to different microphysical parameterizations at different spatial model

20 resolution. In Fig.13 the LWP for the different supersaturation calculations and grid spacing is shown.

We note, that for all grid spacings the the major difference persists between the case using saturation adjustment, which produces a maximum value of approximately $30\,\mathrm{g\,m}^{-2}$ for the LWP in comparision to the explicit and prognostic method
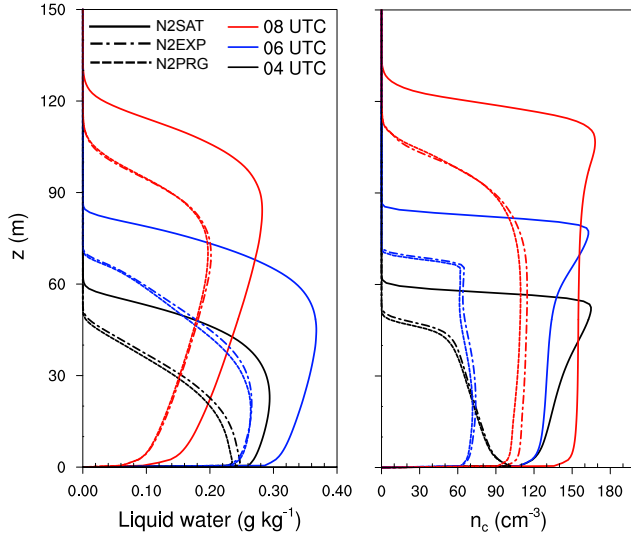
Figure 12. Profiles for liquid water mixing ratio and droplet number concentration at 0400 UTC, 0600 UTC and 0800 UTC.
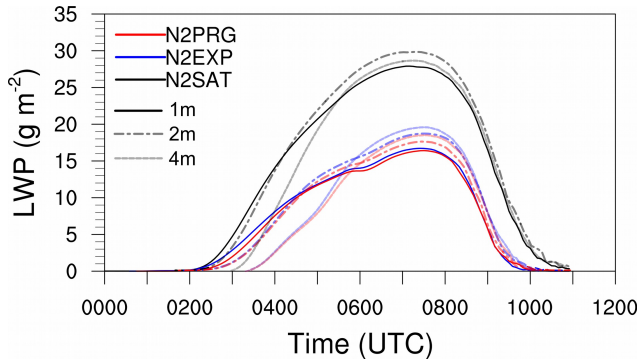
Figure 13. As Fig. 11 but also 2 m (dot-dashed) and 4 m (dashed).

which both exhibit a maximum of approximately $20\,\mathrm{g\,m^{-2}}$. However, interestingly, the relative differences (ratio of N2EXP to N2PRG) in the LWP between the explicit and prognostic methods increases as the grid spacing gets larger. Quantitatively speaking, in case of 1 m grid spacing the relative difference of the LWP is 2.1% between N2EXP and N2PRG during the mature phase while for the case with a grid spacing of 4 m it reaches 8.1%. This increase of the relative changes might be explained by

5   the fact that the explicit scheme is very sensitive to small errors (e.g. induced by the numerical advection) in the fields of T and q_v (e.g. Morrison and Grabowski, 2008; Thouron et al., 2012). A coarser spatial resolution favors that the error introduced by spurious supersaturation gets larger. Due to that we suppose that the increased differences (see Fig. 13) by larger grid spacings are induced by spurious supersaturation, which affect the CCN activation and by that infuence the LWP of the fog layer. As sedimentation and radiative cooling, which are key processes for fog, are sensitive to the number of activated droplets such

10   errors should be considered.

5 Conclusions

The main objective of this work was to investigate the influence of the choice of the microphysical parameterization used in LES models on the life cycle of simulated nocturnal deep radiation fog under typical continental aerosol conditions. For this purpose we performed a series of LES runs for a typical fog event observed at Cabauw (Netherlands). First, we compared the possible error introduced when using saturation adjustment in comparison with an explicit and prognostic method for calculating the supersaturation for diffusional growth. The results showed that, although the model time step was inappropriate for the assumptions made during saturation adjustment, the differences in LWP are at most 1% and the general life cycle is not affected. This could be attributed to the fact that the typical supersaturations in fog are in the range of a few tenths of a percent, and the resulting absolute differences are too small to induce a further influence on dynamics, microphysics or radiation.

In a second part of our study, the effect of different activation schemes of Twomey (1959), Cohard et al. (1998) and Khvorostyanov and Curry (2006) on the simulated fog life cycle were investigated (cases N1EXP to N3EXP). Even though these parameterizations are very similar, our results indicate that the resulting number of activated aerosols (and consequently the number of droplets), known to be a crucial parameter for the fog development, differed significantly. An analysis of the budgets of n_c and q_l showed that diffusional growth is the major process for generating liquid water, but was found to be independent of the number of droplets and thus comparable in magnitude in all cases. In contrast, the sedimentation rates showed a different behaviour: On the one hand, these were found to be proportional to the liquid water mixing ratio, which is high in cases N1EXP and N3EXP. On the other hand, the sedimentation depends on the mean radius of the droplets, which is higher in the case of fewer activated aerosols (case N2EXP). Overall, this leads to almost identical absolute integral sedimentation rate for the three schemes. However, this means that liquid water is removed by sedimentation more rigorously in case N2 (in relative terms) compared to cases N1EXP and N3EXP. Moreover, we could show that most aerosol activation happens near the surface during the formation phase of the fog, while the maximum number of activated aerosols during the mature phase is located at the top of the fog layer. The latter results from the radiative cooling of the fog top, producing the largest supersaturations. Nevertheless, this radiative cooling, triggers a top-down convective layer, so that the the droplets are well mixed, leading to an evenly distributed number concentration throughout the fog layer. As the sedimentation process and radiative cooling are proportional to the droplet number concentration, case N2EXP shows that the LWP is significantly reduced as a result of smaller droplet number concentrations. Moreover, the time marks of the fog life cycle are also affected: If the fog layer contains a smaller amount of liquid water, lifting and dissipation occur earlier, because less energy is required for evaporation of a thinner fog layer.

At last we investigated the impact of different (commonly used) supersaturation calculations on CCN activation by employing a single activation scheme but using the aforementioned different scheme considering supersaturation. From this study we found that in case of saturation adjustment higher droplet number concentration are produced. The explicit method and the prognostic method instead performed quite similar. However, in a grid spacing sensitivity study we observed that the relative differences between the prognostic and explicit approach increase as the spatial resolution decrease. We assume that this is due to larger errors of spurious supersaturations which lead to higher droplet concentrations and thus also effect the LWP.

In summary, the present study indicates that the choice of the used microphysics parameterization can be a key factor for the simulation of radiation fog. While the effect of applying saturation adjustment in case of assuming a constant droplet number concentration on the diffusional growth is negligible, we recommend to use the prognostic approach to calculate the supersaturations in case of a full two-moment microphysics considering activation. Moreover, the choice of the chosen

5   activation scheme has an noticeable impact of the LWP and fog height. However, we have no means to give advice which activation parameterization performs best.

In order to overcome these limitations of the present study, we plan to revisit this particular fog case using a Lagrangian particle-based approach to simulate the microphysics of droplets which will allow for explicitly simulating the development of the 3D droplet size distribution in the fog layer (e.g. Shima et al., 2009). This approach will also allow to resolve all relevant

10   microphysical processes such as activation and diffusional growth instead of parameterizing them. As such simulations are computationally very expensive, only a very limited number of simulations are feasible at the moment, so that most future numerical investigations will - as in the present work - rely on bulk microphysics parameterizations. Based on the results using the Lagrangian approach, however, we hope to be able to give an educated recommendation on the best choice for such bulk parameterizations.

15   *Code availability.* The PALM model used in this study (revision 2675 and revision 3622) is publicly available on http://palm-model.org/trac/browser/palm?rev=2675 and http://palm-model.org/trac/browser/palm?rev=3622, respectively. For analysis, the model has been extended and additional analysis tools have been developed. The extended code, as well as the used Job-Setups and the used PALM source code are publicly available on https://doi.org/10.25835/0067929. All questions concerning the code-extension will be answered from the authors on request.
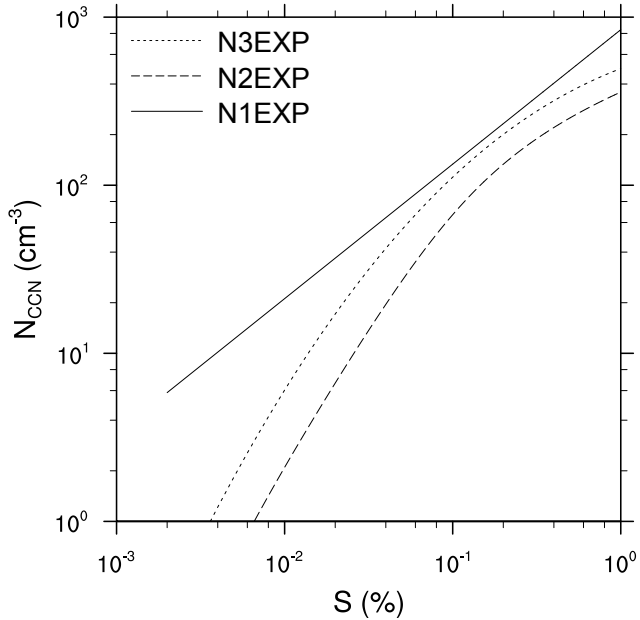
Figure A1. Activation spectrum for three different activation schemes of Twomey (1959)(N1EXP), Cohard et al. (1998)(N2EXP) and Khvorostyanov and Curry (2006)(N3EXP).

Appendix A: Activation spectrum

In Fig. A1 the activation spectrum for the three different activation schemes of Twomey (1959) (N1EXP), Cohard et al. (1998) (N2EXP) and Khvorostyanov and Curry (2006) (N3EXP) are shown.

Author contributions. The numerical experiments were jointly designed by the authors. JS implemented the microphysics parameterizations, conducted the simulations and performed the data analysis. Results were jointly discussed. JS prepared the manuscript, with significant contributions by BM.

Competing interests. The authors declare that they have no conflict of interest.

Acknowledgements. This work has been funded by the German Research Foundation (DFG) under Grant MA 6383/1-1, which is greatly acknowledged. All simulations have been carried out on the Cray XC-40 systems of the North-German Supercomputing Alliance (HLRN, https://www.hlrn.de/).

References

Abdul-Razzak, H. and Ghan, S. J.: A parameterization of aerosol activation: 2. Multiple aerosol types, J. Geophys. Res. Atmos., 105, 6837–6844, 2000.

Ackerman, A. S., VanZanten, M. C., Stevens, B., Savic-Jovcic, V., Bretherton, C. S., Chlond, A., Golaz, J.-C., Jiang, H., Khairoutdinov, M., Krueger, S. K., et al.: Large-eddy simulations of a drizzling, stratocumulus-topped marine boundary layer, Mon. Weather Rev., 137, 1083–1110, 2009.

Árnason, G. and Brown Jr, P. S.: Growth of cloud droplets by condensation: A problem in computational stability, J. Atmos. Sci., 28, 72–77, 1971.

Beare, R. J., Macvean, M. K., Holtslag, A. A., Cuxart, J., Esau, I., Golaz, J.-C., Jimenez, M. A., Khairoutdinov, M., Kosovic, B., Lewellen, D., et al.: An intercomparison of large-eddy simulations of the stable boundary layer, Boundary-Layer Meteorol., 118, 247–272, 2006.

Bergot, T.: Small-scale structure of radiation fog: a large-eddy simulation study, Quart. J. Roy. Meteor. Soc., 139, 1099–1112, 2013.

Boers, R., Baltink, H. K., Hemink, H., Bosveld, F., and Moerman, M.: Ground-based observations and modeling of the visibility and radar reflectivity in a radiation fog layer, J. Atmos. Ocean Technol., 30, 288–300, 2013.

Bott, A.: On the influence of the physico-chemical properties of aerosols on the life cycle of radiation fogs, Boundary-Layer Meteorol., 56, 1–31, 1991.

Bott, A. and Trautmann, T.: PAFOG—a new efficient forecast model of radiation fog and low-level stratiform clouds, Atmos. Res., 64, 191–203, 2002.

Bougeault, P.: Modeling the trade-wind cumulus boundary layer. Part I: Testing the ensemble cloud relations against numerical data, J. Atmos. Sci., 38, 2414–2428, 1981.

Boutle, I., Price, J., Kudzotsa, I., Kokkola, H., and Romakkaniemi, S.: Aerosol-fog interaction and the transition to well-mixed radiation fog, Atmos. Chem. Phys., 18, 7827–7840, 2018.

Clark, T. L.: Numerical modeling of the dynamics and microphysics of warm cumulus convection, J. Atmos. Sci., 30, 857–878, 1973.

Clough, S. A., Shephard, M. W., Mlawer, E. J., Delamere, J. S., Iacono, M. J., Cady-Pereira, K., Boukabara, S., and Brown, P. D.: Atmospheric radiative transfer modeling: A summary of the AER codes, Short Communication, J. Quant. Spectrosc. Radiat. Transfer, 91, 233–244, 2005.

Cohard, J.-M. and Pinty, J.-P.: A comprehensive two-moment warm microphysical bulk scheme. I: Description and tests, Quart. J. Roy. Meteor. Soc., 126, 1815–1842, 2000.

Cohard, J.-M., Pinty, J.-P., and Bedos, C.: Extending Twomey's analytical estimate of nucleated cloud droplet concentrations from CCN spectra, J. Atmos. Sci., 55, 3348–3357, 1998.

Cohard, J.-M., Pinty, J.-P., and Suhre, K.: On the parameterization of activation spectra from cloud condensation nuclei microphysical properties, J. Geophys. Res. Atmos., 105, 11 753–11 766, 2000.

Deardorff, J. W.: Stratocumulus-capped mixed layers derived from a three-dimensional model, Boundary-Layer Meteorol., 18, 495–527, 1980.

Geoffroy, O., Brenguier, J.-L., and Sandu, I.: Relationship between drizzle rate, liquid water path and droplet concentration at the scale of a stratocumulus cloud system, Atmos. Chem. Phys., 8, 4641–4654, 2008.

Geoffroy, O., Brenguier, J.-L., and Burnet, F.: Parametric representation of the cloud droplet spectra for LES warm bulk microphysical schemes, Atmos. Chem. Phys., 10, 4835–4848, 2010.

Gultepe, I., Müller, M. D., and Boybeyi, Z.: A new visibility parameterization for warm-fog applications in numerical weather prediction models, J. Appl. Meteor. Climatol., 45, 1469–1480, 2006.

Gultepe, I., Tardif, R., Michaelides, S., Cermak, J., Bott, A., Bendix, J., Müller, M. D., Pagowski, M., Hansen, B., Ellrod, G., et al.: Fog research: A review of past achievements and future perspectives, in: Fog and Boundary Layer Clouds: Fog Visibility and Forecasting, pp. 1121–1159, Springer, 2007.

Gultepe, I., Hansen, B., Cober, S., Pearson, G., Milbrandt, J., Platnick, S., Taylor, P., Gordon, M., and Oakley, J.: The fog remote sensing and modeling field project, Bull. Amer. Meteor. Soc., 90, 341–359, 2009.

Haeffelin, M., Bergot, T., Elias, T., Tardif, R., Carrer, D., Chazette, P., Colomb, M., Drobinski, P., Dupont, E., Dupont, J.-C., et al.: PARIS-FOG: shedding new light on fog physical processes, Bull. Amer. Meteor. Soc., 91, 767–783, 2010.

Hammer, E., Gysel, M., Roberts, G., Elias, T., Hofer, J., Hoyle, C., Bukowiecki, N., Dupont, J.-C., Burnet, F., Baltensperger, U., et al.: Size-dependent particle activation properties in fog during the ParisFog 2012/13 field campaign, Atmos. Chem. Phys., 14, 10 517–10 533, 2014.

Heus, T., Van Heerwaarden, C., Jonker, H. J., Siebesma, A. P., Axelsen, S., Van Den Dries, K., Geoffroy, O., Moene, A., Pino, D., De Roode, S., et al.: Formulation of the Dutch Atmospheric Large-Eddy Simulation (DALES) and overview of its applications, Geosci. Model Dev., 3, 415, 2010.

Khairoutdinov, M. and Kogan, Y.: A new cloud physics parameterization in a large-eddy simulation model of marine stratocumulus, Mon. Weather Rev., 128, 229–243, 2000.

Khvorostyanov, V. I. and Curry, J. A.: Aerosol size spectra and CCN activity spectra: Reconciling the lognormal, algebraic, and power laws, J. Geophys. Res. Atmos., 111, 2006.

Kokkola, H., Korhonen, H., Lehtinen, K., Makkonen, R., Asmi, A., Järvenoja, S., Anttila, T., Partanen, A.-I., Kulmala, M., Järvinen, H., et al.: SALSA–a Sectional Aerosol module for Large Scale Applications, Atmos. Chem. Phys., 8, 2469–2483, 2008.

Lebo, Z. J., Morrison, H., and Seinfeld, J. H.: Are simulated aerosol-induced effects on deep convective clouds strongly dependent on saturation adjustment?, Atmos. Chem. Phys., 12, 9941–9964, 2012.

Maalick, Z., Kühn, T., Korhonen, H., Kokkola, H., Laaksonen, A., and Romakkaniemi, S.: Effect of aerosol concentration and absorbing aerosol on the radiation fog life cycle, Atmos. Environ., 133, 26–33, 2016.

Maronga, B. and Bosveld, F.: Key parameters for the life cycle of nocturnal radiation fog: a comprehensive large-eddy simulation study, Quart. J. Roy. Meteor. Soc., 2017.

Maronga, B., Gryschka, M., Heinze, R., Hoffmann, F., Kanani-Sühring, F., Keck, M., Ketelsen, K., Letzel, M. O., Sühring, M., and Raasch, S.: The Parallelized Large-Eddy Simulation Model (PALM) version 4.0 for atmospheric and oceanic flows: model formulation, recent developments, and future perspectives, Geosci. Model Dev., 2015.

Mazoyer, M., Lac, C., Thouron, O., Bergot, T., Masson, V., and Musson-Genon, L.: Large eddy simulation of radiation fog: impact of dynamics on the fog life cycle, Atmos. Chem. Phys., 17, 13 017, 2017.

Mensah, A., Holzinger, R., Otjes, R., Trimborn, A., Mentel, T. F., Brink, H. t., Henzing, B., and Kiendler-Scharr, A.: Aerosol chemical composition at Cabauw, The Netherlands as observed in two intensive periods in May 2008 and March 2009, Atmos. Chem. Phys., 12, 4723–4742, 2012.

Morrison, H. and Grabowski, W. W.: Comparison of bulk and bin warm-rain microphysics models using a kinematic framework, J. Atmos. Sci., 64, 2839–2861, 2007.

Morrison, H. and Grabowski, W. W.: Modeling supersaturation and subgrid-scale mixing with two-moment bulk warm microphysics, J. Atmos. Sci., 65, 792–812, 2008.

Nakanishi, M.: Large-eddy simulation of radiation fog, Boundary-Layer Meteorol., 94, 461–493, 2000.

Pruppacher, H. R. and Klett, J. D.: Microphysics of clouds and precipitation, Kluwer Academic Publishers, Dordrecht, Netherlands, 2nd revised edn., 1997.

Seifert, A. and Beheng, K. D.: A double-moment parameterization for simulating autoconversion, accretion and selfcollection, Atmos. Res., 59, 265–281, 2001.

Seifert, A., Khain, A., Pokrovsky, A., and Beheng, K. D.: A comparison of spectral bin and two-moment bulk mixed-phase cloud microphysics, Atmos. Res., 80, 46–66, 2006.

Shima, S., Kusano, K., Kawano, A., Sugiyama, T., and Kawahara, S.: The super-droplet method for the numerical simulation of clouds and precipitation: A particle-based and probabilistic microphysics model coupled with a non-hydrostatic model, Quart. J. Roy. Meteor. Soc., 135, 1307–1320, 2009.

Stolaki, S., Haeffelin, M., Lac, C., Dupont, J.-C., Elias, T., and Masson, V.: Influence of aerosols on the life cycle of a radiation fog event. A numerical and observational study, Atmos. Res., 151, 146–161, 2015.

Thouron, O., Brenguier, J.-L., and Burnet, F.: Supersaturation calculation in large eddy simulation models for prediction of the droplet number concentration, Geosci. Model Dev., 5, 761–772, 2012.

Twomey, S.: The nuclei of natural cloud formation part II: The supersaturation in natural clouds and the variation of cloud droplet concentration, Pure Appl. Geophys., 43, 243–249, 1959.

Wicker, L. J. and Skamarock, W. C.: Time-splitting methods for elastic models using forward time schemes, Mon. Weather Rev., 130, 2088–2097, 2002.

Williamson, J.: Low-storage runge-kutta schemes, J. Comput. Phys., 35, 48–56, 1980.

Zhang, X., Musson-Genon, L., Dupont, E., Milliez, M., and Carissimo, B.: On the influence of a simple microphysics parametrization on radiation fog modelling: A case study during parisfog, Boundary-Layer Meteorol., 151, 293–315, 2014.